GEOPHYSICS, VOL. 77, NO. 5 (SEPTEMBER-OCTOBER 2012); P. WC109–WC122, 15 FIGS., 2 TABLES.
10.1190/GEO2011-0475.1

3D imaging challenges in steeply dipping mining structures: New lights on acquisition geometry and processing from the Brunswick no. 6 seismic data, Canada

Saeid Cheraghi[1], Alireza Malehmir[1], and Gilles Bellefleur[2]

ABSTRACT

We have analyzed and processed a 38-km^2 nonorthogonal 3D surface reflection seismic data in the Brunswick no. 6 area to better understand the effect of acquisition geometry on the resultant image and to provide 3D information about the main geologic structures hosting the mineralization. The 3D data were processed using a conventional prestack dip moveout (DMO) and poststack migration algorithm with special focus on refraction static corrections, velocity analysis, and DMO corrections that are important for the data recorded in crystalline environment. However, the nonorthogonal nature of the 3D data combined with its narrow-azimuth, irregular offset distributions, and 2D nature of midpoint distribution in common depth point bins resulted in a lower quality seismic image than those observed on a series of 2D seismic profiles collected in the area prior to the 3D data acquisition. 2D wavenumber spectrum of the data suggests acquisition footprint associated with the data. Most of the noise associated with the acquisition footprint manifested itself as short-length, high-amplitude shallow reflections but largely were attenuated using a dip filter running in the wavenumber domain. Various bin size and geometries were tested, and the best result was obtained using rectangular bins aligned in the orientation of the shot lines. The processing results indicated that the highly prospective and mineralized Brunswick horizon is part of a continuous reflective package that could guide future deep mineral exploration in this mining camp.

INTRODUCTION

Reflection seismic investigations have proven to be a successful geophysical method in crystalline environment for crustal-scale studies (e.g., Cook et al., 1999; Carbonell et al., 2000; Malehmir et al., 2007, 2009; Dehghannejad et al., 2010; Eaton et al., 2010) and near-surface studies (e.g., Green and Mair, 1983; Juhlin, 1995). One of the early applications of 2D reflection seismic methods in crystalline environment dates back to about 60 years ago (Berson et al., 1956). Although 3D seismic surveys have been recorded in crystalline environment for more than two decades (De Wet and Hall, 1994; Adam et al., 2003), they are not routinely used by the mineral sector. Successful case studies leading to commercial exploitation are required before they can be widely accepted as a practical and efficient exploration tool. Because most shallow deposits have been discovered and exploited, mineral exploration focuses on deeper exploration targets for which reflection seismic methods and their integration with other geologic and geophysical methods can play an important role (Eaton et al., 2003). Several 2D and 3D seismic investigations successfully demonstrated that volcanic-hosted massive sulfide (VHMS) deposits and associated structures can be directly imaged (e.g., Pretorius et al., 1989, 2003; Milkereit et al., 1996, 2000; Adam et al., 2003; Stevenson et al., 2003; Malehmir and Bellefleur, 2009). However, numerous challenges exist from the acquisition to processing and interpretation of data. Low signal-to-noise ratio (S/N) and 3D geologic complexities make the detection of mineralization zones difficult. Although, problems related to crystalline seismic imaging have been discussed previously (e.g., Harrison et al., 2007; Adam et al., 2008; Urosevic et al., 2008), more attention also should be paid to survey designs. Seismic data

Manuscript received by the Editor 28 November 2011; revised manuscript received 23 March 2012; published online 6 September 2012.
[1]Uppsala University, Department of Earth Sciences, Uppsala, Sweden. E-mail: saeid.cheraghi@geo.uu.se; alireza.malehmir@geo.uu.se.
[2]Geological Survey of Canada, Ottawa, Ontario, Canada. E-mail: gbellefl@nrcan-rncan.gc.ca.

should be acquired so that even weak-scattered and reflected waves from ore bodies can be detected.

In a crystalline environment, seismic data usually are processed using prestack dip moveout (DMO) and poststack migration algorithms (e.g., Adam et al., 2003; Malehmir and Bellefleur, 2009). The presence of inadequately sampled 3D data, irregular sampling of offsets and azimuths, and coarse line spacing can generate artifacts on DMO stacked sections (Canning and Gardner, 1988). These artifacts known as the acquisition footprint can lead to wrong interpretations (Marfurt et al., 1998), and cause inexact amplitudes affecting 3D prestack migration results (Gardner and Canning, 1994; Chemingui and Biondi, 1996). Although there are various ways to minimize acquisition footprint on seismic data, a simple solution is to design a dip filter applied in the wavenumber domain to eliminate events that are associated with the acquisition footprint (Gulunay et al., 2006).

The Bathurst Mining Camp in northwest New Brunswick, Canada, hosts several mineral deposits, including the super-giant Brunswick no. 12 and the no. 6 massive sulfide deposits (Figure 1; Wills et al., 2006). The Brunswick no. 12 Zn-Pb-Ag-Cu mine produced more than 229 Mt of sulfide ore (7.66 wt.% Zn, 3.01 wt.% Pb, 0–46 wt.% Cu, and 91 g/t Ag; McCutcheon et al., 2003). The Brunswick no. 6 produced 12.2 Mt of sulfide ore located at relatively shallow depths (5.43 wt.% Zn, 2.15 wt.% Pb, 0.40 wt.% Cu, and 67 g/t Ag; Luff, 1995). This study focuses on the area around the Brunswick no. 6, where in the year 2000, large 3D seismic data were acquired for deep mineral exploration (Figures 1 and 2). Prior to the 3D data, in 1999, Noranda Inc. (now Xstrata) acquired three 2D seismic profiles over the Brunswick no. 6 to assess the general reflectivity of the different geologic formations and investigate the geometry of structures at depth. The 2D data recently were reprocessed and interpreted by Malehmir and Bellefleur (2010) and Cheraghi et al. (2011). The 2D data allowed high-resolution imaging of steeply dipping geologic structures down to 9 km in the crust. Many of the observed reflections reach the surface and correlate with surface geology. In comparison, the 3D data (this study) provide lower-resolution and discontinuous reflections. Acquisition geometry and footprint in the 3D data partly explain this problem.

In this paper, we investigate the discrepancies between the 2D and 3D data by reassessing the acquisition geometry, common depth point (CDP) binning strategy, and data processing used for the Brunswick 3D. The goal is not to criticize previous acquisition and processing parameters, which were selected to satisfy specific exploration objectives, but rather to assess retrospectively their possible impact on the final 3D images. Therefore, the main objectives of this study are (1) to evaluate the acquisition geometry in the Brunswick no. 6 area and its effects on seismic results and (2) to demonstrate and characterize the acquisition footprint in the data. We show that the 3D data contains irregular offset and azimuth distributions with the largest offset range located in a narrow-azimuth band. Such geometry, frequently used in fold and thrust belts (Hope et al., 1995), limits the imaging of many 3D structures clearly observed on the three 2D seismic lines. The choice of a proper CDP binning geometry combined with DMO processing helped in reducing acquisition footprint observed in the 3D data. The example provided in this paper should be instructive for 3D seismic survey designs in a crystalline environment. In particular, care should be taken in obtaining 3D symmetric sampling with an adequate number of closely spaced receivers and shots and an even distribution of offsets and azimuths (Vermeer, 1998).

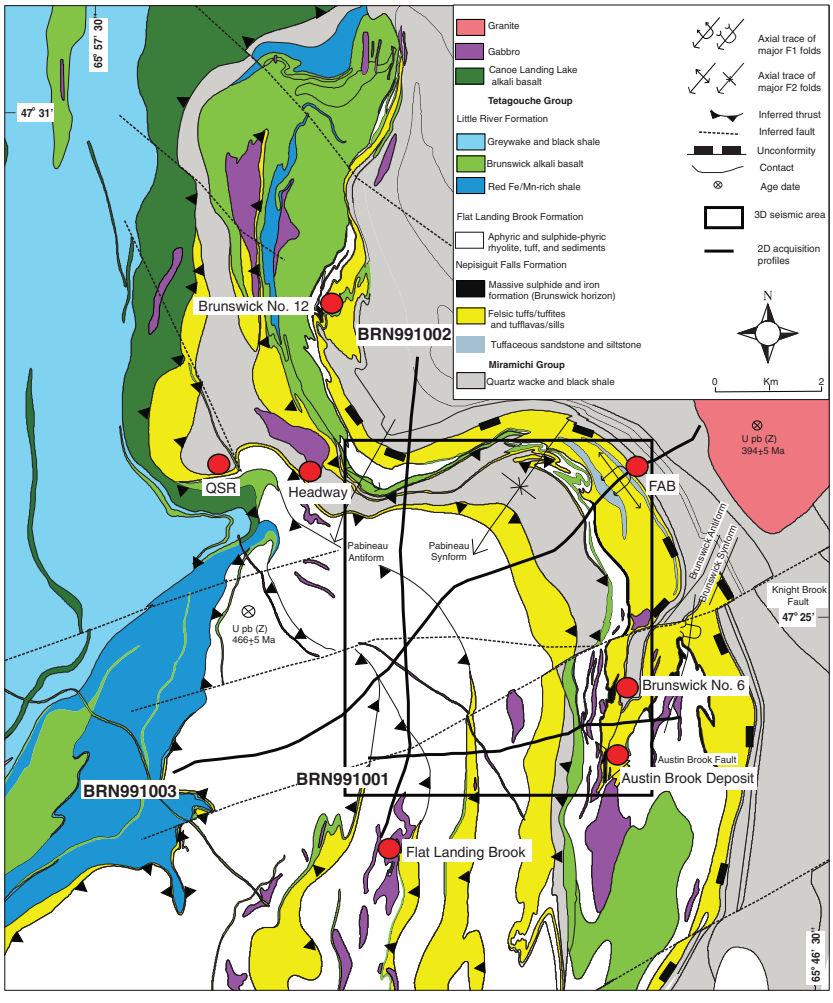

Figure 1. Geologic map of the Brunswick no. 6 area, Bathurst Mining Camp, New Brunswick (modified from van Staal et al., 2003) showing the location of major mineral deposits. The rectangle exhibits the area of the acquired 3D seismic data. The solid black lines are 2D seismic data BRN991001, BRN991002, and BRN991003 acquired in 1999.

GEOLOGIC SETTING

The Brunswick no. 6 is a part of Bathurst Mining Camp, located approximately 27 km southwest of the city of Bathurst, New Brunswick, Canada. The Bathurst Mining Camp is a major base metal producing area in Canada. Tectonically, the Bathurst Mining Camp is made

of several tectonic blocks and slivers that were juxtaposed during the closure of the Tetagouche-Exploits back-arc basin (van Staal et al., 2003). A detailed tectonic history of the Brunswick complex and associated structures of the Bathurst Mining Camp is given by van Staal (1994) and van Staal et al. (2003). A series of oceanic-continental obductions in the early Ordovician and a continent-continent collision in the late Ordovician and Early Silurian are the most important tectonic events in the camp.

In the Brunswick no. 6 area, the oldest rocks belong to the Miramichi Group, a Cambro-Ordovician clastic metasedimentary sequence (van Staal et al., 2003). These rocks are overlain by the middle Ordovician bimodal volcanic and sedimentary rocks of the Tetagouche Group that formed within the Tetagouche-Exploits back-arc basin (van Staal, 1987, 1994; Rogers and van Staal, 1997; Whalen et al., 1998; van Staal et al., 2003), and host the VHMS and iron deposits found in the Brunswick horizon. Iron formation in the Brunswick horizon includes a mixture of sulfide, carbonate, oxide, and silicate facies. This horizon is a key target for geophysical and geochemical exploration in the camp (Gross and McLeod, 1980). The lower part of the Tetagouche Group consists of dominantly felsic volcanic and volcanoclastic rocks of the Nepisiguit Falls Formation, which are overlain by the younger rhyolite flows and rhyolitic volcanic/hyaloclastic rocks of the Flat Landing Brook Formation (Rogers et al., 2003). The youngest part of the Tetagouche Group consists of alkali basalt flows and associated clastic and exhalative sedimentary rocks of the Little River Formation (Figure 1). The total field magnetic map over the study area shown in Figure 2b indicates that the Nepisiguit Falls Formation can be tracked as a moderate to high magnetic formation. Most of the shallow reflections observed on the 2D seismic data are associated with mafic and ultramafic rocks (Cheraghi et al., 2011). The Nepisiguit Falls Formation is a seismic marker horizon characterized by high amplitudes and observed down to a depth of about 4.5 km. Other formations are seismically transparent. Malehmir and Bellefleur (2010) obtained similar results on one of seismic line crossing the Brunswick no. 6 mine (BRN991001). The VHMS deposit in the Brunswick no. 6 (the Brunswick horizon) is related to a steeply dipping reflector package (60°–70°) that can be tracked down to 5 km of the crust (Malehmir and Bellefleur, 2010; Cheraghi et al., 2011). All 2D seismic profiles acquired in this area (Figure 1) provide excellent images of the geology in the upper crust. However, 3D seismic data were required to properly image the folded, faulted, and steeply dipping geologic structures in this area.

3D SEISMIC DATA ACQUISTION

In 2000, Noranda Inc. acquired a 3D dynamite survey over a grid of about 38 km^2 in the Brunswick no. 6 area (Figure 2a). The main objective was to map key mineralization horizons and potentially define new VHMS exploration targets. The survey included 15 shot lines with 400-m line interval, and 28 receiver lines with 290-m line interval. The nominal receiver and shot spacing was 22 m and 60 m, respectively. A total of 1500 shots were recorded in 6-m-deep holes using 0.5 kg of dynamite. Each shot was recorded using vertical geophones distributed in patches with 2367 to 3456 active channels. Table 1 shows the main acquisition parameters used for the 3D seismic data acquisition. The orientation of the shot lines is north–south, whereas receiver lines have an azimuth of 67° (Figure 2a).

The quality of data in raw shot gathers is good and clear first arrivals are often observed at far offset up to 6 km. High-amplitude source-generated noises (e.g., shear wave, ground-roll, and

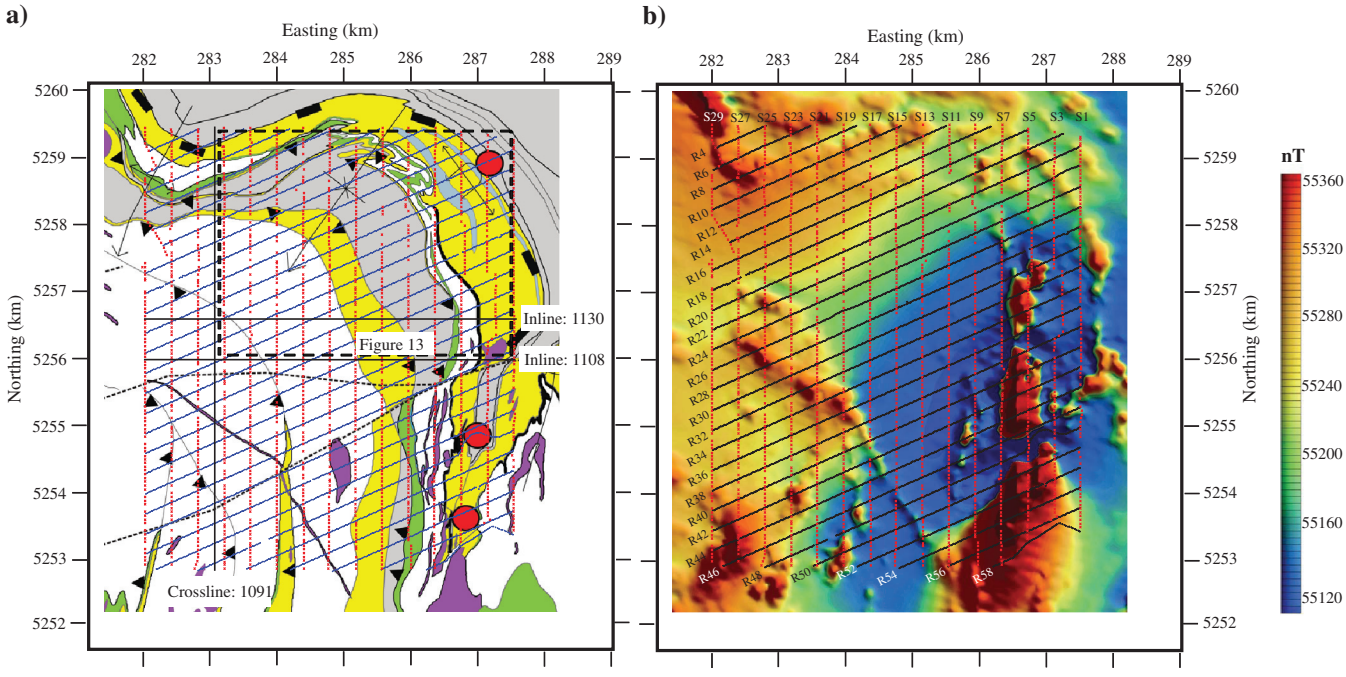

Figure 2. (a) Close-up of the geologic map of the Brunswick no. 6 area showing shot (e.g., S1, S3, S5, . . .) and receiver lines (e.g., R4, R6, R8, . . .). The DMO stacked sections along inlines 1108, and 1130 are shown later in this paper. The dashed rectangle shows the horizontal projection of the 3D stacked cube also presented later in this paper. (b) Shot and receivers lines also are shown on total field aeromagnetic map of the study area (courtesy of Xstrata Zinc). Easting and northing coordinates are based on UTM-NAD 83 projection (zone 19).

air-blast) and occasional ambient noise (e.g., rain and wind) are observed in raw shot gathers. Reflections can be identified in some raw shot gathers.

Table 1. Main acquisition parameters for the Brunswick no. 6 3D seismic survey, 2000.

Survey parameters	
Recording system	SERCEL 388
No. of receiver lines	28 lines: R4, R6, R8, . . . , R58
No. of shot lines	15 lines: S1, S3, S5, . . . , S29
Receiver-line interval	290 m
Shot-line interval	400 m
Maximum source-receiver offset	6700 m
Survey area	38 km^2
Source	Dynamite
Spread parameters	
Receiver spread array	12 lines × 288 active channels
Receiver (group) interval	22 m
Source interval	60 m
Recording length	3 s
Sampling rate	2 ms
Receiver and source parameters	
Geophone type	Mark UM-2, 6/TR
Geophone frequency	10 Hz
Type of base	6" Marsh spike
Source pattern	Single hole
Shot depth	6 m
Charge size	0.5 kg
No. of shots	1500

Figure 3. A raw shot gather recorded in (a) receiver lines R18–R24, (b) receiver lines R26–R32, and (c) receiver lines R34 to R40. A close up of the data along receiver line 32 (R32) is shown later.

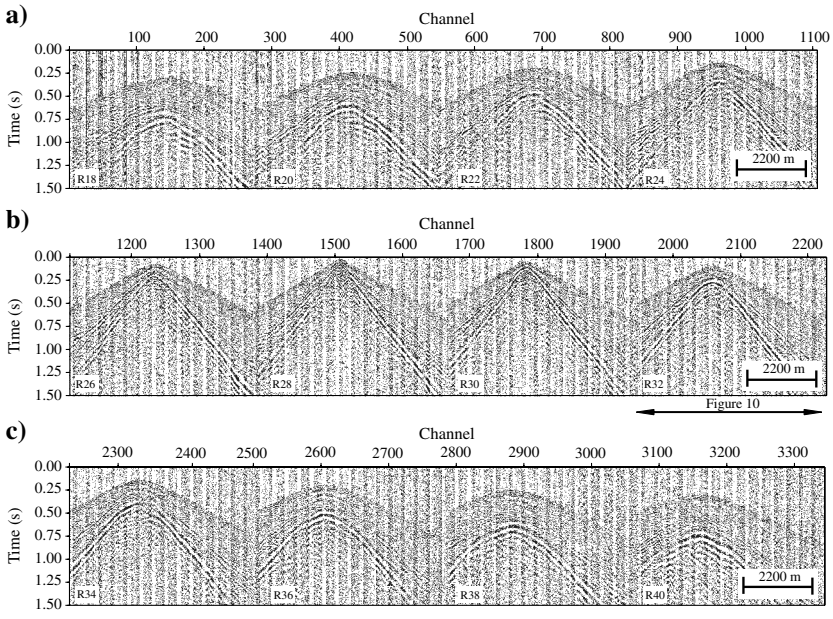

Figure 3 shows a typical raw shot gather recorded in the 3D data. The amplitude spectrum of most shot gathers (an example is shown later in the paper) shows frequencies ranging between 15 and 120 Hz. The figure also demonstrates the low S/N often characteristic of a crystalline environment. The ground-roll and direct shear-wave energy are mainly observed in the frequency band below 30 Hz.

Review of the Brunswick 3D acquisition geometry

A total of 17 patches were used to collect the 3D data (Figure 4). For each patch, 12 southwest–northeast-oriented receiver lines were active. The patches were advanced from south-to-north one receiver line at a time. A new patch was formed by adding a new receiver line to the north while deactivating the southernmost receiver line (Figure 4). Every new patch covered 90% of the previous patch in terms of number of receivers or receiver lines. As receiver lines were moved to the north, shot lines were also moved to the north but confined within only two receiver lines with the exception of patches 1, 14, and 17. This resulted in almost 10% shot coverage per patch. The shot salvos for patches 1 and 17 (Figure 4) covered 50% of their respective patch area and contain the largest number of shot points. Patches 15 and 16 have the lowest number of shot points (Figure 4).

Potential problems

The nonorthogonal 3D geometry used for the Brunswick no. 6 survey is not typically acquired in a crystalline environment. Here, we explain the advantages and disadvantages of this geometry in comparison with the more common orthogonal geometry. We use the term "rack" to define a set of shot points of the same shot line between two receiver lines (Morrice et al., 2001). The design will be split-spread if an equal number of receiver lines are located on each side of the rack over the orthogonal patch. Because the maximum offset in the inline and the crossline directions at the center of the split-spread patch are the same, the distribution of midpoint traces has an equal length in both directions and provides

wide-azimuth geometry (Vermeer, 1998). When the patch is orthogonal but rectangular in shape, the maximum inline offset at the center of the patch is larger than maximum crossline offset; the midpoint distribution will be as well rectangular and the patch shows narrow-azimuth geometry. In the case of a nonorthogonal geometry with only few shots fired at the center of the patch, trace midpoint distribution shows narrow-azimuth geometry and the orientation of midpoint traces will be in the direction of the receiver lines. The main advantage of narrow-azimuth geometry compared with the wide-azimuth geometry is that for the same survey coverage, the narrow geometry builds fold faster up to the maximum crossline offset (Vermeer, 1998). Whether the geometry is orthogonal or nonorthogonal, rectangular or square patch, sequential patches should partially overlap each other to cover the entire survey area. A 50% overlap for receivers and shots is common.

Vermeer (1998) defines the aspect ratio of a patch as the ratio of maximum inline offset and maximum crossline offset. An aspect ratio of one implies a symmetric sampling and a wide-azimuth patch. The patch aspect ratio for almost all patches of the Brunswick 3D is much higher than one, implying that the 3D data are narrow azimuth.

Figure 5 shows source-receiver offset and azimuth distributions for the Brunswick no. 6 3D survey. Maximum offset of 6.5 km (Figure 5a) suggests that steeply dipping reflector can be detected. The offset-azimuth plot (Figure 5b) demonstrates that majorities of the midpoints traces follow a narrow-azimuth distribution oriented in the northeast–southwest direction. Benefits of such acquisition geometry include:

- The northeast–southwest narrow-azimuth character of the 3D data was designed to be perpendicular to the strike of main geologic structures observed in the central and eastern side of the survey area.
- Larger offsets obtained in the northeast–southwest direction are suitable to image steeply dipping structures typically found in the Brunswick area.
- Larger number of active channels in combination with nonorthogonal geometry can compensate for the lower number of shots (explosive) and thus, helped maintain a low acquisition cost while meeting the survey objectives (i.e., the steeply east-dipping Brunswick horizon).

However, this geometry is not suitable to image the generally steep south-dipping structures observed in the northern part of 3D survey area. Such structures were mapped at surface and were clearly identified on the north–south 2D seismic line located in the northwestern part of the 3D area (Cheraghi et al., 2011). Figure 5b

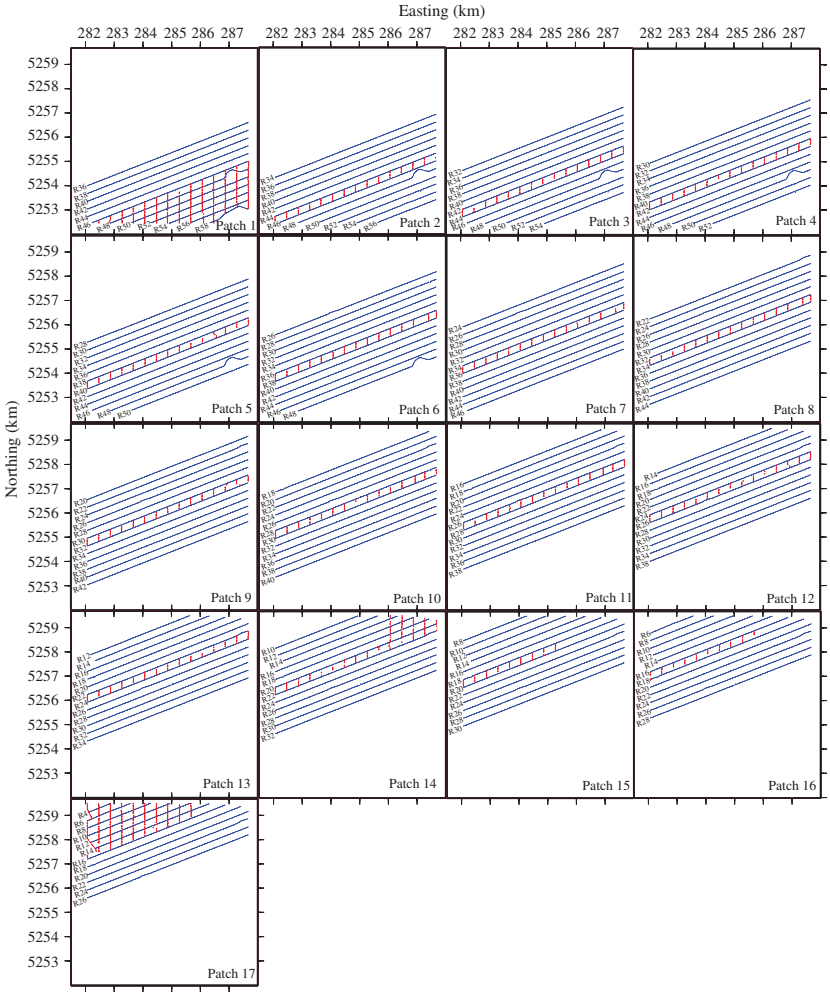

Figure 4. The 3D seismic patches used to acquire the seismic data (Figure 2) over the Brunswick no. 6 area. The blue dots are active receiver lines and the red dots are active shot points in each patch.

shows that only short offsets are available in the dip direction of those structures, so imaging of steep dips can only be poor.

DESIGN OF 3D CDP BINS

The nonorthogonal geometry offers several CDP binning geometry. In this section, we test various binning options and select the one producing the best stacking results. The optimal CDP bin size for a dipping reflector is theoretically calculated by following formula (Yilmaz, 2001):

$$\Delta x \leq \frac{V_{\text{rms}}}{4 f_{\text{max}} \sin \alpha}, \tag{1}$$

where V_{rms} defines the rms average velocities above the target reflector, α is the dip of the geologic structure, and f_{max} is the maximum nonaliased frequency to resolve the target reflector. Sonic logs and 2D seismic data in the Brunswick no. 6 area indicate V_{rms} ranging between 5500 and 6000 m/s and a maximum reflector dip of 60°–70° (Malehmir and Bellefleur, 2010; Cheraghi et al., 2011). The amplitude spectrum of the 3D data shows a maximum useful frequency of 120 Hz. Based on these values, we estimate that a bin size between 10 and 30 m would be suitable for the Brunswick 3D data.

To choose the best CDP bin orientation and size, we tested two scenarios. In the first scenario (scenario A), CDP bins are parallel to the shot lines with inlines in the east–west direction (Figure 6a and 6b). In the second scenario (B), CDP bins are parallel to the receiver lines with inlines directed toward northeast–southwest (Figure 6c and 6d). We also considered square and rectangular bins with different sizes (15–30 m) for scenarios A and B (Figure 6). We generated DMO stacked volume for each scenario and compared the resultant images to help in the selection of the optimal binning geometry. A time slice of DMO stacked cube at 880 ms with bin size of 11 by 30 m for scenarios A and B is presented in Figure 6a and 6c, respectively. The same time slice for the bin size of 30 by 30 m of

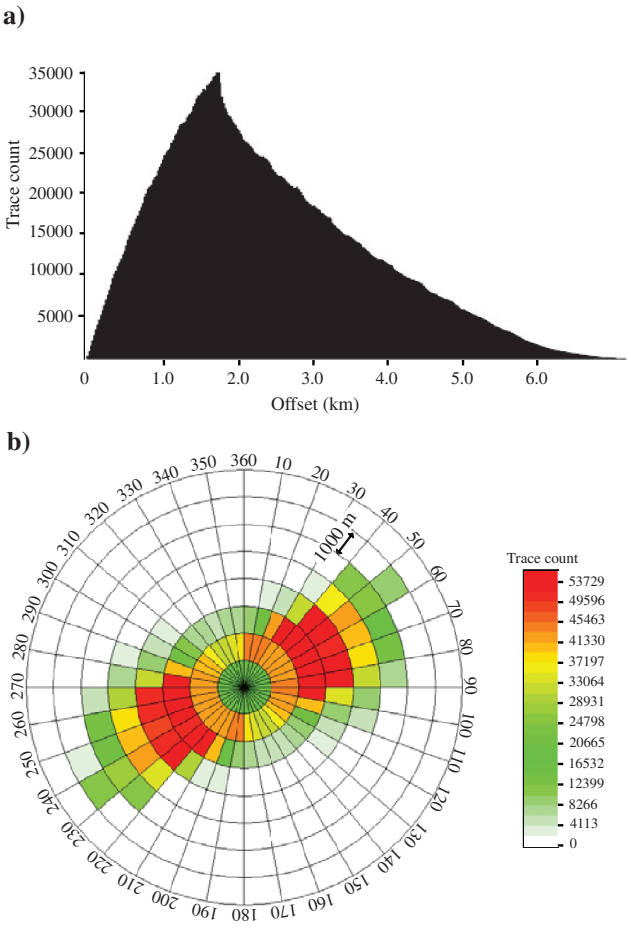

Figure 5. (a) Source-receiver offset distribution. (b) Azimuth-offset coverage for the Brunswick 3D data. The offset step over sequential circles is 1000 m. Traces within 10° azimuth sector are grouped together for display purposes.

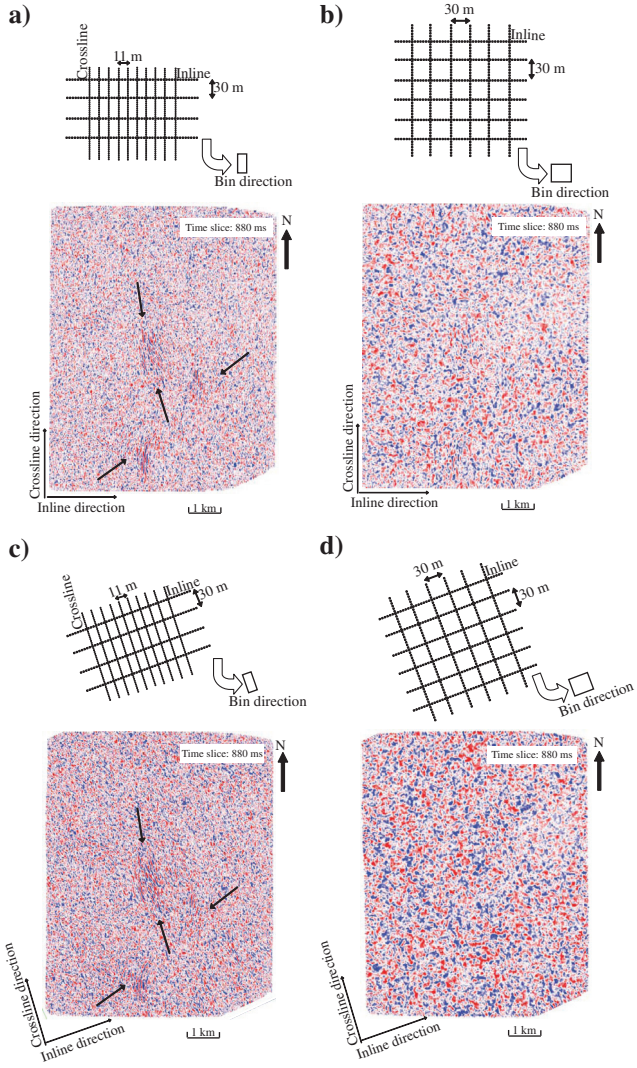

Figure 6. A time slice extracted from the DMO stacked cube at 880 ms shown for (a) scenario A using CDP bin size of 11 m (inline) by 30 m (crossline), (b) scenario A using CDP bin size of 30 m (inline) by 30 m (crossline), (c) scenario B using CDP bin size of 11 m (inline) by 30 m (crossline), and (d) scenario B using CDP bin size of 30 m (inline) by 30 m (crossline).

both scenarios is shown in Figure 6b and 6d. Based on this analysis, scenarios A and B with bin size of 11 by 30 m (Figure 6a and 6c) produce comparable images in the time slice. However, for the entire processed cube, scenario A with CDP bins of 11 by 30 m (Figure 6a) provided a better image than scenario B. Results for CDP bins of 30 by 30 m of both scenarios (Figure 6b and 6d) were not as convincing as those obtained using bin size of 11 by 30 m. Although a bin size of 30 by 30 m allowed higher fold and more uniform offset distribution, the resulting DMO stack had lower resolution, and therefore, this bin geometry was excluded for the final processing.

CDP fold coverage for the first three different tests (Figure 6a–6c) is shown in Figures 7, 8, and 9, respectively. Examples of midpoint

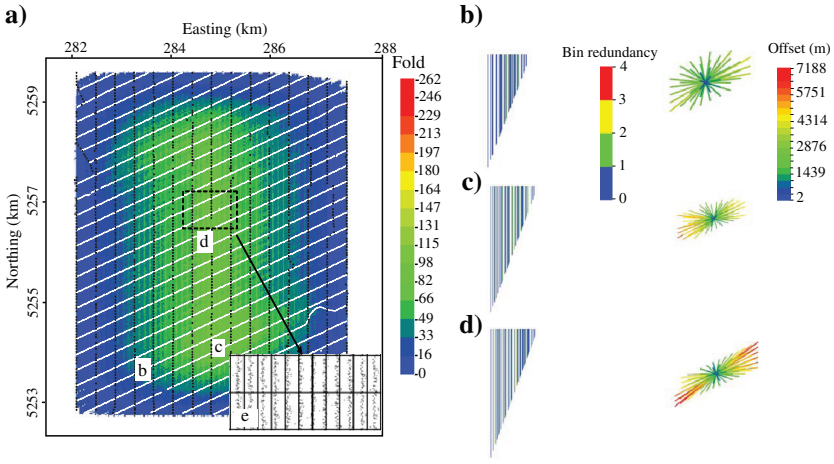

Figure 7. (a) CDP fold coverage for the scenario A (Figure 6a) using CDP bin size of 11 m (inline) by 30 m (crossline); (b, c, and d) show the bin-offset redundancy (repeated number of offsets in the bin) and bin-azimuth (azimuth of each offset value in the bin) graphs for the bins b, c, and d shown in (a). See inset e for distribution of trace midpoints for the dashed area shown in (a).

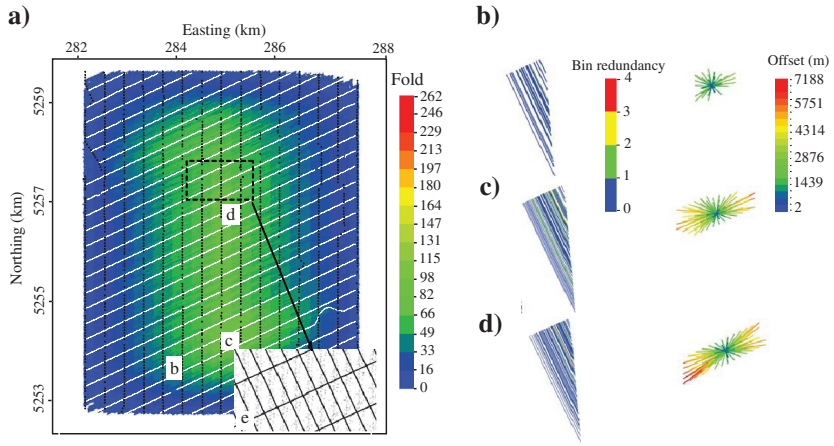

Figure 8. (a) CDP fold coverage of scenario B (Figure 6c) using CDP bin size of 11 m (inline) by 30 m (crossline); (b, c, and d) are the bin-offset redundancy and bin-azimuth graphs for the bins b, c, and d shown in (a). See inset e for distribution of trace midpoints for the dashed area shown in (a).

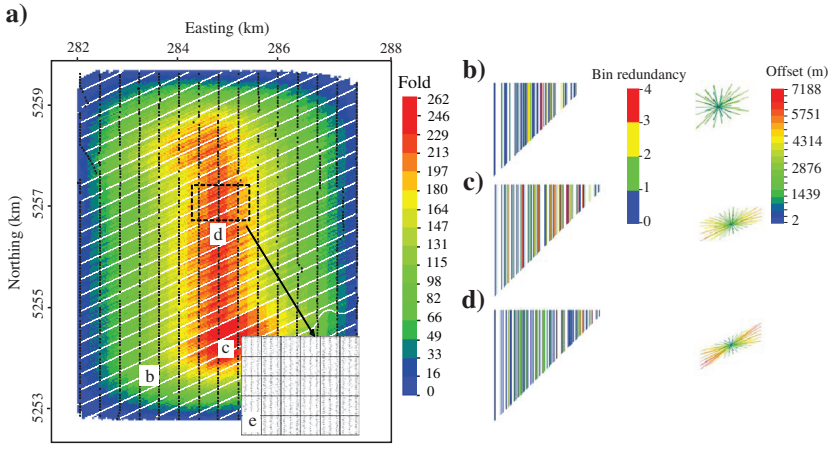

Figure 9. (a) CDP fold coverage of scenario A (Figure 6b) using CDP bin size of 30 m (inline) by 30 m (crossline); (b, c, and d) are the bin-offset redundancy and bin-azimuth graphs for the bins b, c, and d shown in (a). See inset e for distribution of trace midpoints for the dashed area shown in (a).

spread from the central part of the 3D survey area also are shown (e.g., Figure 7e) and indicate a north–south directed midpoint spread almost over the entire part of the survey area. Bin-offset redundancy (repeated number of offsets within a bin) and bin-azimuth distributions also are plotted for each scenario (e.g., Figure 7b–7d). The bin-azimuth graph (known as spider graph) exhibits the orientation of offset values for three selected bins (see b, c, and d on Figures 7a, 8a, and 9a), showing examples from lowfold and high-fold areas.

Figure 7 presents our preferred CDP bin geometry (scenario A with 11 by 30 m bin; see Figure 6a). This binning geometry generally shows a uniform CDP fold of about 65 in the central part of the survey area (Figure 7a). The spider and the offset redundancy plots for three points inside the survey area suggest a relatively uniform but narrow-offset distribution as expected from the data (Figure 7b–7d). The spider plot is symmetric only in the southern margins of the survey area and shows a wide-azimuth distribution for offsets up to 4000 m. The bin redundancy plot, however, shows gaps (white parts) indicating missing offset values in the plot. Almost similar conclusion can be drawn for point c (see Figure 7c). The spider plot shows narrow-azimuth distribution for the maximum long offset of 5500 m, whereas the bin redundancy plot also shows gaps and a few repeating values in short to moderate offsets. Offset distribution for a bin located in the central part of the survey area (see d in Figure 7) shows the highest fold and relatively continuous distribution of short offsets. Missing offsets generally are observed in moderate to long distances. As expected, the spider plot shows long offsets mostly in the northwest–southeast direction (Figures 7d and 5b). In general, each CDP bin includes traces only from one midpoint line (see inset e in Figure 7a).

The fold coverage map for scenario B with CDP bins of 11 by 30 m is shown in Figure 8a. A higher CDP fold coverage is obtained in this case. This geometry generally includes traces mostly from two different midpoint lines per bin (see inset e in Figure 8a). The lower quality seismic DMO brute stack volume shown in Figure 6c could likely result from smearing effects or stacking of midpoint traces belonging to different subsurface regions. We recognize that depth midpoints obtained with ray tracing would be more appropriate for this analysis. However, the complex and poorly understood geology at depth, which is often the case in crystalline environment, prevent the construction of a realistic geologic model. Thus, trace midpoints instead of depth midpoints were used for the design of the bins.

The CDP fold coverage map for scenario A with the 30 by 30 m bin size (see Figure 6b) is shown in Figure 9a. Obviously, this binning geometry provides the highest fold. However, a few missing offsets and azimuths are evident in the spider and offset plots (Figure 9b–9d). The central bins still show a narrow-azimuth behavior despite the larger CDP bin. Each CDP bin almost always covers traces from three midpoint lines (see inset e in Figure 9a). The lowest quality DMO stack shown in Figure 6b also could be explained due to the smearing effects.

Nevertheless, a drawback of rectangular bins is that they can introduce migration aliasing in the shorter direction in the bins. With the current bin geometry, we expect that frequencies above 120 Hz (reflector dipping at about 60°) and 55 Hz are aliased in the inline and crossline directions, respectively. This is a fundamental data limitation that applies to any migration algorithms.

Table 2. Processing sequence of the Brunswick no. 6 3D data, 2011.

Step	Parameters
1	Read 2.0 s SEG-Y data
2	Build geometry data (several tests for CDP bin size)
3	Trace editing and polarity reversal
4	Pick first breaks: full offset range, automatic neural network algorithm but manually inspected and corrected
5	Refraction static, replacement velocity 5200 m/s, V0 1000 m/s
6	Geometric-spreading compensation: V^2t
7	Time variant band-pass filtering (10–30–120–150 Hz)
8	Surface-consistent deconvolution: filter length 80 ms, gap 14 ms, white noise 0.1%
9	Top mute: 20 ms after first break
10	Direct shear-wave attenuation (near-offset)
11	Air blast attenuation
12	Trace balance using data window
13	Velocity analysis (iterative): Every fifth CDP inline and crossline
14	Residual static corrections (iterative)
15	NMO corrections: 30% stretch mute
16	3D DMO corrections
17	Stack
18	Dip filter in the wavenumber domain
19	Fxy-deconvolution: inline and crossline directions
20	Phase shift migration: Inline and crossline direction

SEISMIC DATA PROCESSING

To process the 3D seismic data, we considered a processing flow similar to the one used for the 2D data (Malehmir and Bellefleur, 2010; Cheraghi et al., 2011). Table 2 shows the principal processing steps used for the processing. Shear-wave and ground-roll noise were attenuated with the application of a band-pass filter (Figure 10b). Surface-consistent deconvolution with an 80-ms operator length and a 14-ms gap length helped to increase the coherency of reflections and reduce source wavelet effect (Figure 10b). Past experience with the 3D acquired in crystalline environment shows that near-surface low-velocity layer has a significant effect on the misalignment of reflected waves, and thus, properly implemented refraction static corrections are important to improve the alignment of reflections and enhance S/N (Adam et al., 2003; Bergman et al., 2006; Schijns et al., 2009). To estimate refraction static corrections, we picked approximately five million first arrivals using an automatic neural network algorithm followed by manual editing and corrections where needed. Three-dimensional refraction static corrections were calculated for all traces using a one-layer low-velocity model. An rms misfit of about 4 ms was obtained. After the application of the refraction static corrections, the continuity of reflections is improved (Figure 10c).

We used the picked first arrivals to design a trace-top mute function to remove direct P-wave and refracted energy but made sure

that near surface or wide-angle reflections that can be correlated with surface geology were preserved in the data (Figure 10d).

Our previous experience from the processing of the 2D lines indicated that most of the subsurface structures are steeply dipping, therefore requiring high stacking velocity. Velocities ranging from 5000 to 10000 m/s were tested to obtain normal moveout (NMO) corrected shot gathers. The selected stacking velocities ranged from 5000 to 7500 m/s. The NMO corrected gathers were used to estimate residual static corrections (Malehmir and Juhlin, 2010) that helped to enhance coherency of reflections in the shot gathers (Figure 10d) and NMO-corrected stacked cube. A 3D Kirchhoff DMO with variable velocity model ranging from 5000 to 6200 m/s was used to obtain a dip-independent velocity function (Hale and Artley, 1993). DMO-corrected data were later stacked to produce an unmigrated cube of the study area.

Evidence and attenuation of acquisition footprint

The 2D character of the midpoint distribution within CDP bins (Figure 7) raised some concerns about the presence of significant acquisition footprint in the 3D data. Our visual inspection of time slices at the shallow traveltime did not demonstrate this. To further investigate this possibility, we transformed the trace midpoint locations to wavenumber frequency domain and searched for indications of acquisition footprint. Gulunay et al. (2006) showed that spatially periodic nature of acquisition footprint forms spikes in the wavenumber domain. Signal will be located in the center of the spectrum where $k_x = k_y = 0$, whereas repetitive noise (periodic noise) caused by acquisition will appear as nonzero wavenumber spikes superimposed on the signal spectrum. Following Gulunay et al. (2006), we obtained $k_x - k_y$ spectrum by first sorting traces within each bin according to offset range. Each offset range is equal to the minimum bin dimension. Each range for all bins is considered as a slice that is transformed from the x-y domain to the wavenumber domain ($k_x - k_y$) by applying a 2D fast Fourier transform. The procedure is repeated for all slices, and then all slices are stacked together. The magnitude of stacked values is calculated to obtain the amplitude spectrum (Cordsen et al., 2000). Figure 11 shows a series of $k_x - k_y$ spectra of trace midpoint distributions from the four scenarios discussed before. Periodic noise is observed in the data in all

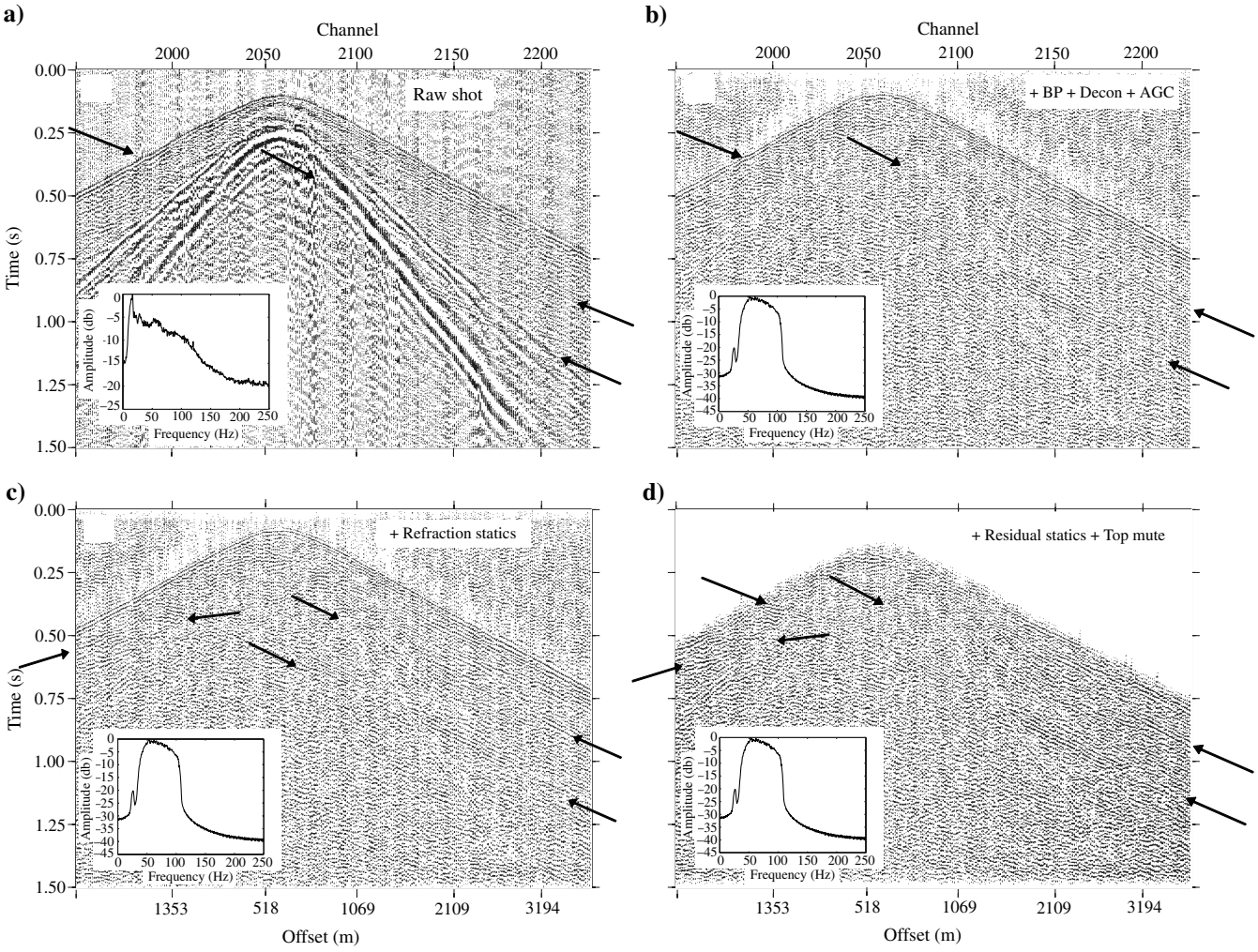

Figure 10. A close up of the raw shot gather shown in Figure 3 for the data recorded along receiver line 32 (R32); (a-d) shows increase in the S/N and coherency of a series of steeply dipping reflections after various processing steps. Note the increase in the continuity of the reflections marked by the black arrows after various processing steps. Insets show graphs of amplitude spectrums after different processing steps.

the four scenarios. We observe that the 11 by 30 m bin geometry of scenario A (Figure 11a) shows less noise periodicity problem than the other scenarios. Although the 30 by 30 m bin for scenario B shows the strongest signal (Figure 11d), it also is characterized with the strongest periodic noise. Fortunately, most of the artifacts associated with the acquisition footprint manifest themselves as short, mostly horizontal to gently dipping events in the shallow part of the seismic cube. Velocity analysis and poststack filter, such as *Fxy*-deconvolution (see Table 2) did not remove the effect of the acquisition footprint. Interferences between reflections and footprint effects in the stacked cube can be reduced by a separation of these two components in the inline or time slice direction of the wavenumber domain (e.g., Marfurt et al., 1998; Hindriks and Duijndam, 2000; Gulunay et al., 2006). To reduce footprint effect, we applied a dip filter in the wavenumber domain that attenuates almost all horizontal reflections. The dip filter does not affect the steeply dipping geologic structures mapped in the study area. The continuity and strength of the reflections are markedly improved after the application of the dip filter (Figure 12). Figure 13a and 13b shows a perspective view of the processed cube before and after the application of the dip filter.

PROCESSING RESULTS AND INTEPRETATION

Although the 3D seismic cube has relatively a lower seismic quality in comparison with the 2D data, numerous reflections can be followed close to the surface allowing correlation with the surface geology. Previous interpretations from the 2D data because they provide higher quality images near the surface, also were used to guide the interpretation of the 3D data (e.g., Malehmir and Bellefleur, 2010; Cheraghi et al., 2011). Previous interpretations established that the prospective Brunswick horizon is located within packages comprising several reflections. Finite-difference modeling results suggested that the Brunswick horizon could generate a high-amplitude reflection on seismic image; however, this horizon could not be specifically distinguished in the reflection package without the support of well-logging and geologic data (Cheraghi et al., 2011). On the 3D, two packages of reflections also observed on the 2D reach the surface where the Nepisiguit Falls Formation is exposed (P1 and P2 in Figures 12 and 13b). The reflective character of the Nepisiguit Falls Formation previously demonstrated in well-logging data available in the study area explains packages P1 and P2 (Malehmir and Bellefleur, 2010). The P1 and P2 reflective packages also may contain reflections from the Brunswick horizon, which occurs in the footwall of the Nepisiguit Falls Formation. This observation is important for defining and guiding deep mineral exploration strategies. In particular, seismic results help to distinguish areas of no or weak reflectivity (low mineralization potential) from areas of high reflectivity (high mineralization potential) for future deep mineral exploration. The P1 and P2 reflective packages extend down to at least 4–5 km depth (Figure 13b), implying that they are regional and crustal scale geologic features. The Nepisiguit Falls Formation

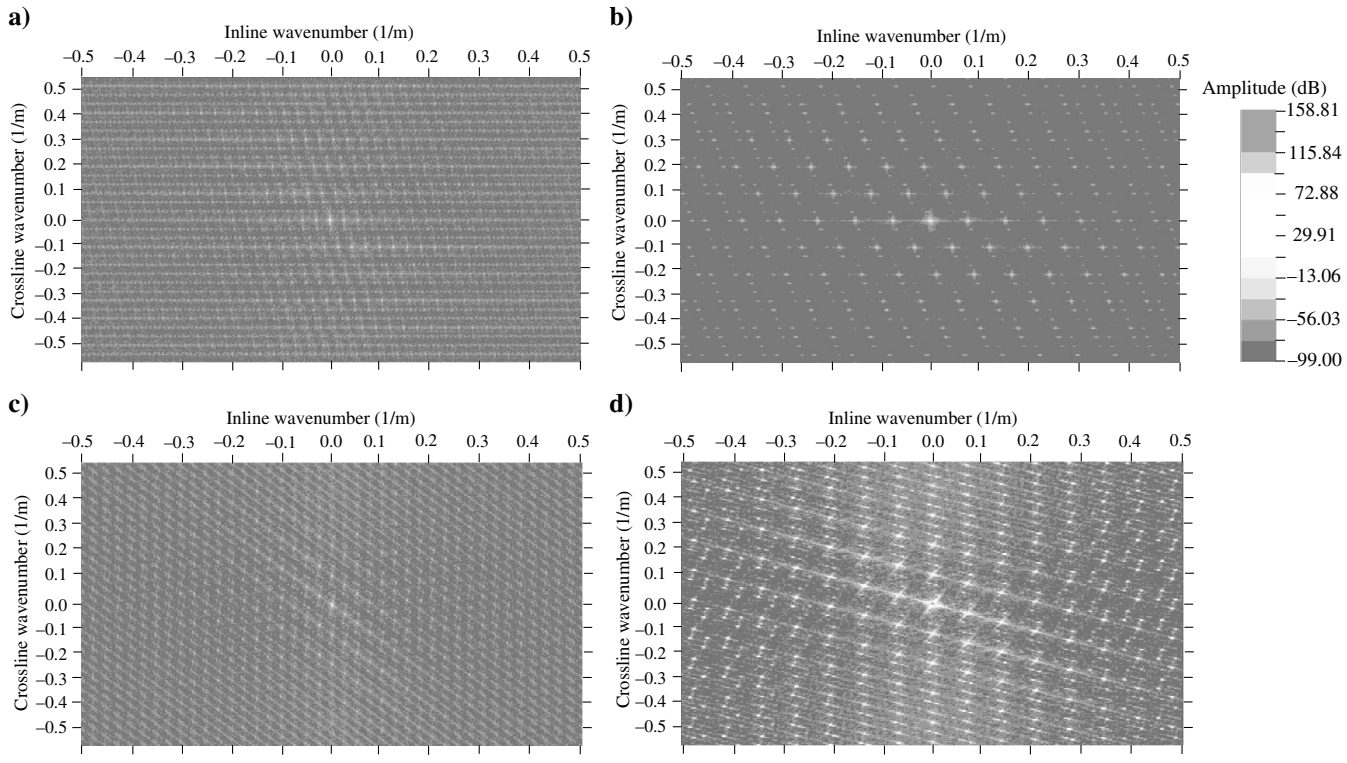

Figure 11. Two-dimensional ($k_x - k_y$) transformation of trace midpoints into frequency wavenumber domain of (a) bin size of 11 m (inline) by 30 m (crossline) of scenario A (Figure 6a), (b) bin size of 30 m (inline) by 30 m (crossline) of scenario A (Figure 6b), (c) bin size of 11 m (inline) by 30 m (crossline) of scenario B (Figure 6c), and (d) bin size of 30 m (inline) by 30 m (crossline) of scenario B (Figure 6d). For display purpose a gray scale is used (see the color bar).

and associated structures have a regional high magnetic signature that also can be easily correlated to the P1 and P2 reflection packages at the surface (Figure 2).

A set of deep crustal reflections marked as I1 is observed from approximately the central part of the seismic cube all the way to the northern part (Figure 13b). These high-amplitude but relatively gently dipping reflections also were observed on the 2D profiles BRN991002 and BRN991003. They are attributed to ultramafic rocks located beneath the Bathurst Mining Camp volcanic and sedimentary rocks east of the mining camp (see Rogers et al., 2003).

Figure 14 shows a 3D perspective view of the migrated seismic volume with the available 3D geologic model of the study area. To make a comparison, the 3D surfaces representing the Nepisiguit Falls Formation (the reflective package in the processed cube containing reflection P1 and P2) are presented. The 3D surfaces are defined from surface geologic maps and borehole intersections. The 3D seismic data partly and locally imaged the Nepisiguit Falls Formation.

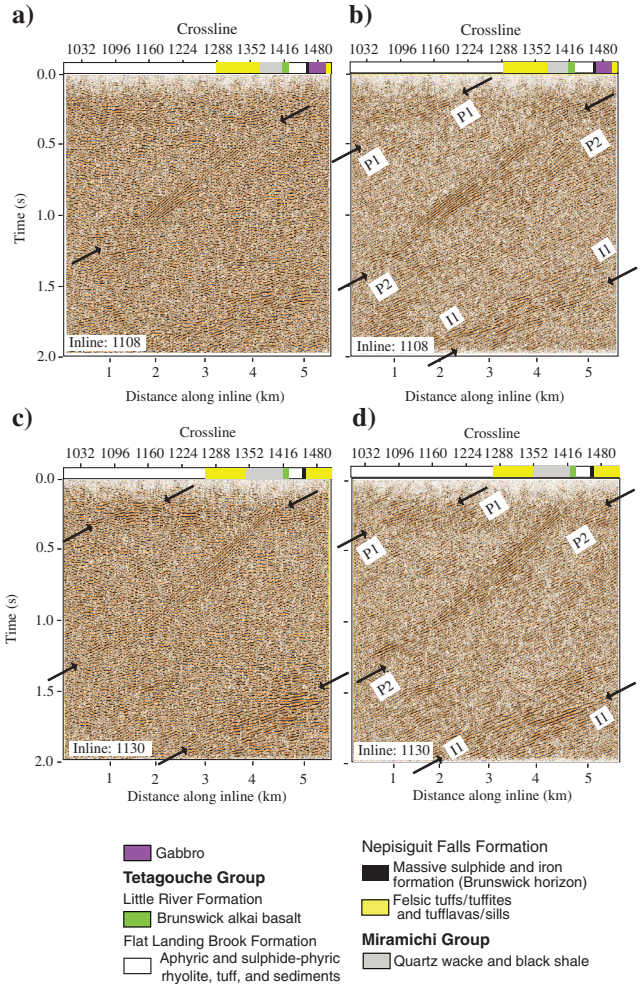

Figure 12. DMO stacked sections of inline 1108 (a) before and (b) after applying the dip filter. DMO stacked sections of inline 1130 (c) before and (b) after applying the dip filter. See Figure 2 for the locations of inlines 1108 and 1130. See text for interpretation of events marked as P1, P2, and I1.

DISCUSSION

Figure 15 shows comparisons between the unmigrated and migrated stacks along the BRN991003 2D line that crosses the Brunswick no. 6 mine, and an unmigrated and migrated cross section extracted from the 3D data along BRN991003. The 2D data produced higher-resolution image and provides more details near the surface than the 3D data. However, the steeply dipping reflection P2 and deep reflection I1 are clearly visible on the unmigrated and migrated data from the 3D cube (Figure 15). The high-amplitude reflection R1 observed at shallow depth on Figure 15a (stacked

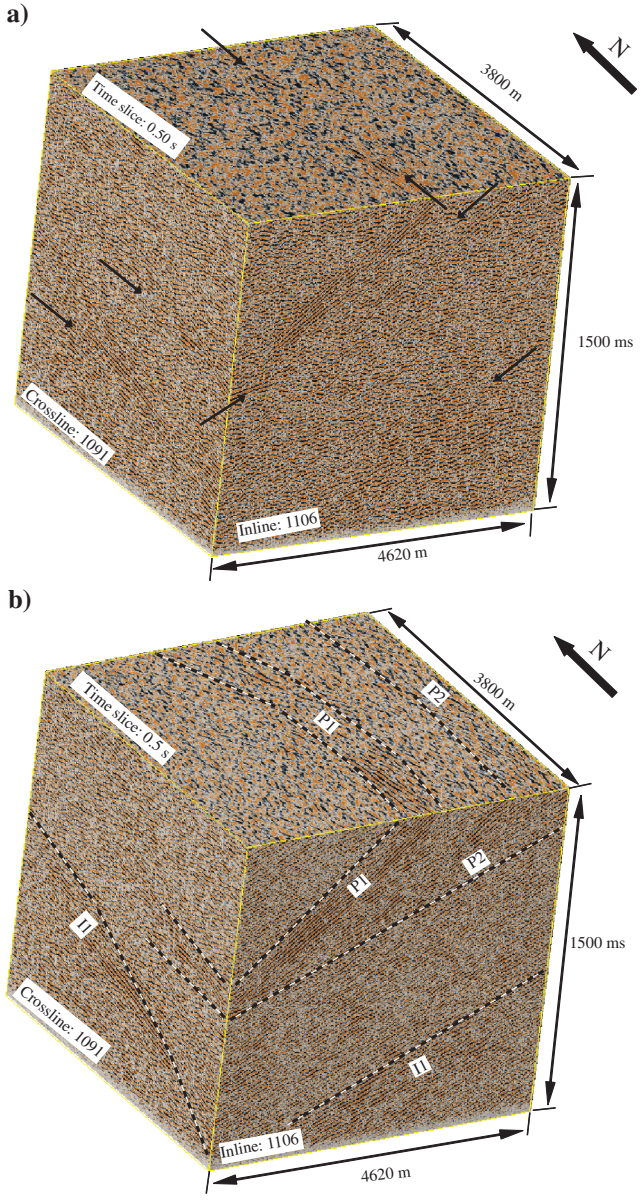

Figure 13. A portion of the DMO stacked cube shown for inline 1106, crossline 1091, and time slice 500 ms (a) before and (b) after application of the dip filter. See Figure 2 for the surface projection of the cube. See text for interpretation of events marked as P1, P2, and I1.

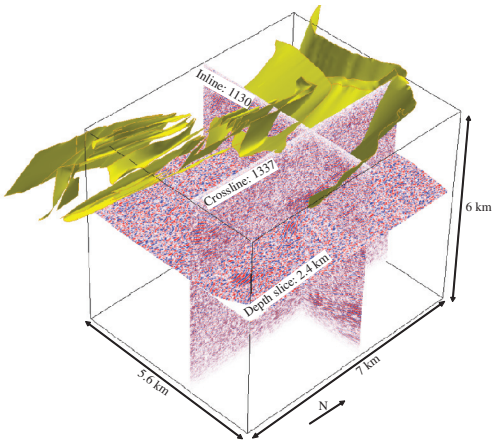

Figure 14. Three-dimensional perspective view of inline 1130, crossline 1330, and a depth slice 2.4 km with the geologic model of the Nepisiguit Falls Formation (courtesy of Xstrata zinc).

section) and 15c (migrated section) and generated by mafic/ultramafic rocks (gabbro/basalt, see Cheraghi et al., 2011) is not observed on the 3D data shown in Figure 15b (stacked section) and 15c (migrated section). There are fundamental differences between the 2D data and 3D data that have been discussed by Vestrum and Gittins (2009). Two-dimensional profiles provide a high-resolution section of shallow subsurface structures, which can be correlated with surface geologic map. Three-dimensional seismic data can image lateral variations of subsurface formations and allow for out-of-the-plane reflections to migrate properly. For Brunswick data, the differences between the 2D and 3D data are likely due to the acquisition setup and the complex geology.

There are very specific reasons that justified the acquisition parameters used for this survey. In particular, the Brunswick horizon in the eastern part of the 3D grid was the key target, and thus, dictated the orientation of the receiver lines. Spacing between shot and receiver lines aimed at imaging large mineralization zones. Small

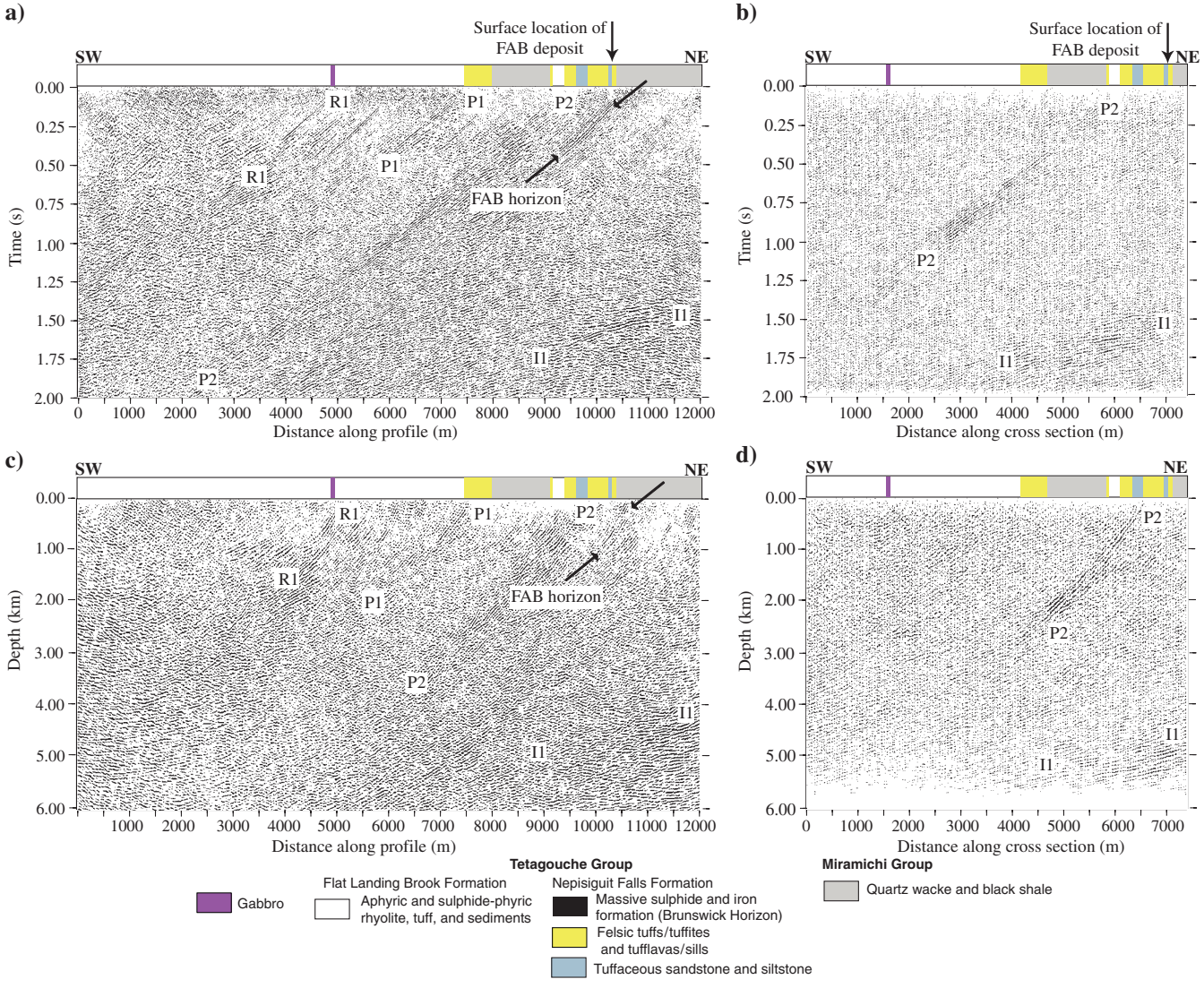

Figure 15. Comparison between (a) stacked sections along the BRN991003 2D profile (Figure 1; Cheraghi et al., 2011) and (b) a cross section extracted from the unmigrated stacked volume along the BRN991003 2D profile. Similar comparison also is shown for (c) migrated 2D line and (d) and 3D data along the 2D profile. See text for interpretation of P1, P2, R1, and I1.

noneconomical mineral deposits that might not show up on the final seismic cube were not considered as worthwhile targets. In addition to this, financial consideration and logistic issues likely influenced the choice of the acquisition parameters. The large range of offsets distributed in the general dip direction over the Brunswick no. 6 area allows to map laterally continuous subsurface formations. However, the limited north–south offset range does not allow proper imaging of steeply south-dipping sulfide sheets that could be associated with the Brunswick horizon in the northern part of the survey. Other acquisition parameters that likely influenced the quality of the 3D data include the large shot/receiver line interval and shot point spacing of about three times than the receiver point spacing.

Although there are sophisticated methods for attenuating the acquisition footprint, the problem of sparsity of the data and the 2D midpoint distribution in CDPs cannot be easily solved by processing. Trace interpolation or mixing would very likely be challenged by the complex nature of geology and low S/N in shot gathers (Kaplan et al., 2010).

The CDP binning strategy and processing approach used in this paper demonstrates that the reflection package associated with key prospective horizons in the Brunswick no. 6 area could be imaged on the 3D data. However, data processing cannot correct for the low distribution of large offsets in the north–south direction, thus limiting the ability to image steeply south-dipping structures mapped in the northern part of the grid. Such structures also include the prospective Brunswick horizon, which follows a large regional fold (Figure 1). A tighter but more costly survey (shorter shot/receiver lines interval) with symmetric offset distribution, would provide a seismic volume closer to the images obtained on the 2D data and more representative of the 3D geology characterizing this mining camp.

CONCLUSION

The Bathurst Mining Camp exhibits very complex geology with usually steeply dipping and strongly deformed, folded, and altered rocks. This poses a challenge in reflection seismic imaging of mineral deposits and their structures and requires a careful survey design to obtain high-resolution seismic data. The 2D data acquired in this environment shows steeply dipping continuous reflections almost reaching the surface. In comparison, the 3D seismic data are characterized by a lower number of short and discontinuous reflections. The 3D survey was originally designed to image steeply west-to-southwest dipping reflectors possibly related to the Brunswick horizon. Although primary survey objectives were achieved, this geometry setup is not optimal to image steep south dipping reflections expected and observed in the northwest part of the survey area. In particular, the nonorthogonal nature of the 3D data, combined with the narrow-azimuth and irregular offset distribution, the 2D character of the midpoints distribution in CDP bins, the shot and receiver line spacing, and logistic and financial considerations are all parameters that can explain the difference between the 2D and 3D data. High 3D data density (shots and receivers) is essential in a crystalline environment to obtain high-resolution seismic images of the shallow structures.

We tested several CDP binning scenarios and found that an 11 by 30 m bin oriented along the shot line directions provided the best brute stacked volumes. Data processing with this bin geometry improved the imaging of reflections associated with key exploration targets in the Brunswick no. 6 area. Our processing approach included refraction static corrections, coherent and random noise filtering as well as DMO corrections. Periodic noise related to acquisition footprint was identified with wavenumber spectrum analysis and attenuated using a dip filter applied in the wavenumber domain. The final seismic cube shows a series of reflective and transparent packages that now have characteristics similar to the reflections observed on the 2D data. The Brunswick horizon is located within a laterally continuous reflective package that may help and guide future deep mineral exploration in this area.

The retrospect analysis of the Brunswick no. 6 3D acquisition geometry and processing demonstrates once again that survey design strongly influences final seismic image of the subsurface. This influence is even more significant in steeply dipping, severely folded and faulted geologic environments often characterizing VHMS mining camps.

ACKNOWLEDGMENTS

The authors thank Xstrata for providing access to the seismic data in the Brunswick no. 6 area. Saeid Cheraghi wishes to thank Iranian Academic Center for Education, Culture, and Research (ACECR); Isfahan University of Technology Branch for funding his research Ph.D. position. This work is a joint collaboration between Uppsala University and the Geological Survey of Canada. GLOBE ClaritasTM was used for the seismic data processing. GMT from P. Wessel and W.H.F. Smith was used to prepare some of the figures. GEDCO is thanked for providing an academic license of OMNI3D used in this study. We are grateful for the constructive comments and suggestions provided by four anonymous reviewers and the associate editor B. Milkereit. Geological Survey of Canada contribution 20110403.

REFERENCES

Adam, E., E. L'Heureux, E. Bongajum, and B. Milkereit, 2008, 3D seismic imaging of massive sulfides: Seismic modeling, data acquisition and processing issues: 78th Annual International Meeting, SEG, Expanded Abstracts, 3621–3624.

Adam, E., G. Perron, G. Arnold, L. Matthews, and B. Milkeriet, 2003, 3D seismic imaging for VMS deposit exploration, Matagami, Quebec, *in* D. W. Eaton, B. Milkereit, and M. H. Salisbury, eds., Hardrock seismic exploration: SEG.

Bergman, B., A. Tryggvason, and C. Juhlin, 2006, Seismic tomography studies of cover thickness and near-surface bedrock velocities: Geophysics, **71**, no. 6, U77–U84, doi: 10.1190/1.2345191.

Berson, I. S., G. N. Pariiskaya, and S. P. Starodubrovskaya, 1956, Recording high frequency reflected waves on the Russian platform: Bulletin of Academy of Science: USSR, Geophysics Series, No. 6.

Canning, A., and G. H. F. Gardner, 1988, Reducing 3-D acquisition footprint for 3-D DMO and 3-D prestack migration: Geophysics, **63**, 1177–1183, doi: 10.1190/1.1444417.

Carbonell, R., J. Gallart, A. Pérez-Estaún, J. Diaz, S. Kashubin, J. Mechie, F. Wenzel, and J. Knapp, 2000, Seismic wide-angle constrains on the crust of the southern Urals: Journal of Geophysical Research, **105**, 13755–13777, doi: 10.1029/2000JB900048.

Chemingui, N., and B. Biondi, 1996, Handling irregular geometry in wide azimuth surveys: 66th Annual International Meeting, SEG, Expanded Abstracts, 32–35.

Cheraghi, S., A. Malehmir, and G. Bellefleur, 2011, Crustal-scale reflection seismic investigations in the Bathurst Mining Camp, New Brunswick, Canada: Tectonophysics, **506**, 55–72, doi: 10.1016/j.tecto.2011.04.011.

Cook, F. A., A. J. van der Velden, K. W. Hall, and B. J. Roberts, 1999, Frozen subduction in Canada's Northwest Territories: Lithoprobe deep lithospheric reflections profiling of the western Canadian Shield: Tectonics, **18**, 1–24, doi: 10.1029/1998TC900016.

Cordsen, A., M. Galbraith, and J. Peirce, 2000, Planning land 3D seismic surveys: SEG.

Dehghannejad, M., C. Juhlin, A. Malehmir, P. Skyttä, and P. Weihed, 2010, Reflection seismic imaging of the upper crust in the Kristineberg mining

area, northern Sweden: Journal of Applied Geophysics, **71**, 125–136, doi: 10.1016/j.jappgeo.2010.06.002.
De Wet, J. A. J., and D. A. Hall, 1994, Interpretation of the Oryx 3-D seismic survey, *in* Anhauser, C. R., ed., 15th CMMI Congress, **3**, 259–270.
Eaton, D. W., E. Adam, B. Milkereit, M. Salisbury, B. Roberts, D. White, and J. Wright, 2010, Enhancing base-metal exploration with seismic imaging, in Lithoprobe: Parameters, processes and the evolution of a continent: Canadian Journal of Earth Sciences, **47**, 741–760, doi: 10.1139/E09-047.
Eaton, D. W., B. Milkereit, and M. Salisbury, 2003, Seismic methods for deep mineral exploration: Mature technologies adapted to new targets: The Leading Edge, **22**, 580–585, doi: 10.1190/1.1587683.
Gardner, G. H. F., and A. Canning, 1994, Effects of irregular sampling on 3D pre-stack migration: 64th Annual International Meeting, SEG, Expanded Abstracts, 1553–1556.
Green, A. G., and J. A. Mair, 1983, Subhorizontal fractures in a granitic pluton — Their detection and implications for radioactive waste disposal: Geophysics, **48**, 1428–1449, doi: 10.1190/1.1441428.
Gross, G. A., and C. R. McLeod, 1980, A preliminary assessment of the chemical composition of iron formations in Canada: The Canadian Mineralogist, **18**, 223–229.
Gulunay, N., N. Benjamin, and M. Magesan, 2006, Acquisition footprint suppression on 3D land surveys: First Break, **24**, 71–77.
Hale, D., and C. Artley, 1993, Squeezing dip moveout for depth-variable velocity: Geophysics, **58**, 257–267, doi: 10.1190/1.1443410.
Harrison, C. B., M. Urosevic, and E. Stoltz, 2007, Processing, inversion and multi attribute analysis of the intrepid seismic line at the St. Ives gold camp, Western Australia: 77th Annual International Meeting, SEG, Expanded Abstracts, 1928–1932.
Hindriks, K., and A. J. W. Duijndam, 2000, Reconstruction of 3D seismic signals irregularly sampled along two spatial coordinates: Geophysics, **65**, 253–263, doi: 10.1190/1.1444716.
Hope, C., P. Kong, and D. Flentge, 1995, 3D geometry for overthrust areas: The Leading Edge, **14**, 715–719, doi: 10.1190/1.1437156.
Juhlin, C., 1995, Imaging of fracture zones in the Finnsjön area, central Sweden, using the seismic reflection method: Geophysics, **60**, 66–75, doi: 10.1190/1.1443764.
Kaplan, S. T., M. Naghizadeh, and M. D. Sacchi, 2010, Data reconstruction with shot-profile least-squares migration: Geophysics, **75**, no. 6, WB121–WB136, doi: 10.1190/1.3478375.
Luff, W. M., 1995, A history of mining in the Bathurst area, northern New Brunswick, Canada: The Canadian Institute of Mining, Metallurgy and Petroleum Bulletin, **88**, 63–68.
Malehmir, A., and G. Bellefleur, 2009, 3D seismic reflection imaging of VHMS deposits, Insights from re-processing of the Halfmile Lake data, New Brunswick, Canada: Geophysics, **74**, no. 6, B209–B219, doi: 10.1190/1.3230495.
Malehmir, A., and G. Bellefleur, 2010, Reflection seismic imaging and physical properties of base-metal and associated iron deposits in the Bathurst Mining Camp, New Brunswick, Canada: Ore Geology Reviews, **38**, 319–333, doi: 10.1016/j.oregeorev.2010.08.002.
Malehmir, A., and C. Juhlin, 2010, An investigation of the effects of the choice of stacking velocities on residual statics for hardrock reflection seismic processing: Journal of Applied Geophysics, **72**, 28–38, doi: 10.1016/j.jappgeo.2010.06.008.
Malehmir, A., C. Schmelzbach, E. Bongajum, G. Bellefleur, C. Juhlin, and A. Tryggvason, 2009, 3D constraints on a possible deep >2.5 km massive sulfide mineralization from 2D crooked- seismic reflection data in the Kristineberg mining area, northern Sweden: Tectonophysics, **479**, 223–240, doi: 10.1016/j.tecto.2009.08.013.
Malehmir, A., A. Tryggvason, H. Lickorish, and P. Weihed, 2007, Regional structural profiles in the western part of the Palaeoproterozoic Skellefte Ore District, northern Sweden: Precambrian Research, **159**, 1–18, doi: 10.1016/j.precamres.2007.04.011.
Marfurt, K. J., R. M. Scheett, J. A. Sharp, and M. G. Harper, 1998, Suppression of the acquisition footprint for seismic sequence attribute mapping: Geophysics, **63**, 1024–1035, doi: 10.1190/1.1444380.
McCutcheon, S. R., W. M. Luff, and R. W. Boyle, 2003, The Bathurst Mining Camp, New Brunswick, Canada: History of discovery and evolution of geologic models: Economic Geology, **11**, 17–35.
Milkereit, B., E. K. Berrer, A. R. King, A. H. Watts, B. Roberts, E. Adam, D. W. Eaton, J. Wu, and M. H. Salisbury, 2000, Development of 3-D seismic exploration technology for deep nickel-copper deposits — A case history from the Sudbury basin, Canada: Geophysics, **65**, 1890–1899, doi: 10.1190/1.1444873.
Milkereit, B., D. W. Eaton, J. Wu, G. Perron, M. H. Salisbury, E. Berrer, and G. Morrison, 1996, Seismic imaging of massive sulfide deposits: Part II. Reflection seismic profiling: Economic Geology, **91**, 829–834, doi: 10.2113/gsecongeo.91.5.829.
Morrice, D. J., A. S. Kenyon, and C. J. Beckett, 2001, Optimizing operations in 3-D land seismic surveys: Geophysics, **66**, 1818–1826, doi: 10.1190/1.1487124.
Pretorius, C. C., A. Jamison, and C. Irons, 1989, Seismic exploration in the Witwatersrand Basin, Republic of South Africa. Proceedings of Exploration 87, Ontario Geologic Survey, Spec. 3, 241–253.
Pretorius, C. C., M. R. Muller, M. Larroque, and C. Wilkins, 2003, A review of 16 years of hardrock seismics on the Kaapvaal Craton, *in* D. W. Eaton, B. Milkereit, and M. H. Salisbury, eds., Hardrock seismic exploration: SEG.
Rogers, N., and C. R. van Staal, 1997, Comparing the Bathurst Mining Camp to the Japan Sea and Okinawa Trough: Ancient, recent, and active back-arcs [abs.]: Geological Association of Canada-Mineralogical Association of Canada Annual Meeting, Abstract, **22**, A–127.
Rogers, N., C. R. van Staal, J. A. Winchester, and L. R. Fyffe, 2003, Provenance and chemical stratigraphy of the sedimentary rocks of the Miramichi, Tetagouche, California Lake and Fournier groups, northern New Brunswick, *in* W. D. Goodfellow, S. R. McCutcheon, and J. M. Peter, eds., Massive sulfide deposits of the Bathurst Mining Camp, New Brunswick, and Northern Maine: Economic Geology, Monograph, **11**, 111–128.
Schijns, H., S. Heinonen, D. R. Schmitt, P. Heikkinen, and I. T. Kukkonen, 2009, Seismic refraction traveltime inversion for static corrections in a glaciated shield rock environmental case study: Geophysical Prospecting, **57**, 997–1008, doi: 10.1111/gpr.2009.57.issue-6.
Stevenson, F., R. M. A. Higgs, and R. J. Durrheim, 2003, Seismic imaging of precious and base-metal deposits in Southern Africa, *in* D.W. Eaton, B. Milkereit, and M. H. Salisbury, eds., Hardrock seismic exploration: SEG.
Urosevic, M., A. Kepic, C. Juhlin, and E. Stolz, 2008, Hard rock seismic exploration of ore deposits in Australia: 78th Annual International Meeting, SEG, Expanded Abstracts, 3613–3614.
van Staal, C. R., 1987, Tectonic setting of the Tetagouche group in northern New Brunswick: Implications for plate tectonic models of the northern Appalachians: Canadian Journal of Earth Sciences, **24**, 1329–1351, doi: 10.1139/e87-128.
van Staal, C. R., 1994, Brunswick subduction complex in the Canadian Appalachians: Record of the Late Ordovician to Late Silurian collision between Laurentia and the Gander margin of Avalon: Tectonics, **13**, 946–962, doi: 10.1029/93TC03604.
van Staal, C. R., R. A. Wilson, N. Rogers, L. R. Fyffe, J. P. Langton, S. R. McCutcheon, V. McNicoll, and C. E. Ravenhurst, 2003, Geology and tectonic history of the Bathurst Supergroup, Bathurst Mining Camp and its relationships to coeval rocks in southwestern New Brunswick and adjacent Maine — A synthesis, *in* W. D. Goodfellow, S. R. McCutcheon, and J. M. Peter, eds., Massive sulfide deposits of the Bathurst Mining Camp, New Brunswick, and Northern Maine: Economic Geology, Monograph, **11**, 37–60.
Vermeer, G. J. O., 1998, 3D symmetric sampling: Geophysics, **63**, 1629–1647, doi: 10.1190/1.1444459.
Vestrum, R., and J. Gittins, 2009, Technologies from foothills seismic imaging: replacement or complements?: First Break, **27**, 61–66.
Whalen, J. B., N. Rogers, C. R. van Staal, F. J. Longstaffe, G. A. Jenner, and J. A. Winchester, 1998, Geochemical and isotopic (Nd, O) data from the Ordovician felsic plutonic and volcanic rocks of the Miramichi Highlands: Petrogenetic and metallogenic implications for the Bathurst Mining Camp: Canadian Journal of Earth Sciences, **35**, 237–252, doi: 10.1139/e97-102.
Wills, A. O., D. R. Lentz, and G. Roy, 2006, Chemostratigraphy at the Brunswick No. 6 volcanic-sediment-hosted massive sulfide deposit, New Brunswick: Resolving geometry from drill core in deformed felsic volcanic rocks: Exploration and Mining Geology, **15**, 35–51, doi: 10.2113/gsemg.15.3-4.35.
Yilmaz, O., 2001, Seismic data analysis: Processing, inversion, and interpretation of seismic data: SEG.